Chemical Science

ROYAL SOCIETY OF CHEMISTRY

EDGE ARTICLE

View Article Online
View Journal | View Issue

Cite this: *Chem. Sci.*, 2024, **15**, 11928

All publication charges for this article have been paid for by the Royal Society of Chemistry

Received 17th April 2024
Accepted 24th June 2024

DOI: 10.1039/d4sc02550d

rsc.li/chemical-science

Ordered assembly of two different metal clusters with the same topological connectivity in one single coordination network†

Jian-Wei Cao, ‡ Tao Zhang, ‡ Juan Chen, Jin-Bo Wang, Yu Wang and Kai-Jie Chen *

The introduction of heterogeneous components within one single coordination network leads to the multifunctionality of the final material. However, it is hard to precisely control the local distribution of these different components in such a coordination network, especially for different components with identical topological connectivity. In this study, we successfully achieved the ordered assembly of $[Mn_3(\mu_3\text{-}O)]$ nodes and $[Mn_6(\mu_3\text{-}O)_2(CH_3COO)_3]$ nodes within one pacs coordination network. The resulting new structure (**NPU-6**) with heterogeneous metal nodes simultaneously inherits the advantages of both parent networks (good thermal stability and high pore volume). The significant effect of the reaction concentration of competing ligand CH_3COO^- on the mixed assembly of these two nodes in **NPU-6** is revealed by a series of control experiments. This method is anticipated to offer a valuable reference for orderly assembling heterogeneous components in coordination networks.

Introduction

Metal–organic frameworks (MOFs),[1] also known as porous coordination polymers (PCPs)[2] and metal–organic materials (MOMs),[3] can be systematically designed by targeting the structure through reticular chemistry and crystal engineering strategies. Currently there are over 100 000 hits in the Cambridge Structural Database (CSD) MOF subset,[4] which have been widely used in the field of gas storage/separation, sensing, energy storage, *etc.*[1,5–14] Most MOFs are composed of a single type of ligand and a single type of metallic secondary building unit (SBU),[15–18] which however limit their structural diversity and functional versatility. By introducing multiple components within the parent network,[19,20] the resulting structurally heterogeneous MOFs, the so-called multivariate MOFs (MTV-MOFs), reported by Yaghi *et al.*[21,22] or solid solution reported by Kitagawa *et al.*,[23–25] can largely enhance the structural diversity and functional versatility of MOF contents.[26–29] Although as many as ten kinds of metal ions[30] and eight kinds of organic ligands[22] can be incorporated within one MOF crystal, the local distribution of heterogeneous contents is hard to control and recognize.[31,32] In most cases, these components are arranged randomly, or as short/long duplicates or insertions,[33] and the long-range ordered arrangement of heterogeneous components within one single coordination network has been still a great challenge yet.[34,35] Things will become much more difficult if these heterogeneous components are topologically identical.

We realize that introducing heterogeneities that are largely chemically distinguishable would be a practical way, not only because the distinguishable natures make heterogeneities recognizable but also because self-recognition and self-assembly of heterogeneities would make the ordered arrangement of multiple components possible, even when these heterogeneous components share the same topological connectivity. In 2015, Bu[36] and Chen[37] demonstrated the construction of a pacs (partitioned acs) network using a 9-connected $[M_3(\mu_3\text{-}O)]$ triangle trimer. In 2021, our group found that a brand-new double-decker topologically 9-connected $[Mn_6(\mu_3\text{-}O)_2(CH_3COO)_3]$ hexamer can also be incorporated within a pacs network (**NPU-1**).[38] And together with our following study,[39] we can reason that the incorporating of CH_3COO^- would be the key for the formation of $[Mn_6(\mu_3\text{-}O)_2(CH_3COO)_3]$. It is possible to realize the mixed assembly of such two clusters with largely different sizes and geometries in one network if we precisely control the concentration of CH_3COO^- and further control the producing rate of these clusters in the reaction media.

Based on the above vision, we selected a trinuclear $[Mn_3(\mu_3\text{-}O)]$ cluster (**CPM-153**)[40] and a hexanuclear $[Mn_6(\mu_3\text{-}O)_2(CH_3COO)_3]$ cluster (**NPU-1**) of model metal clusters for assembly exploration. We successfully realized the assembly of two chemically different but topologically identical

Key Laboratory of Special Functional and Smart Polymer Materials of Ministry of Industry and Information Technology, Xi'an Key Laboratory of Functional Organic Porous Materials, School of Chemistry and Chemical Engineering, Northwestern Polytechnical University, Xi'an, Shaanxi, 710072, China. E-mail: ckjiscon@nwpu.edu.cn

† Electronic supplementary information (ESI) available. CCDC 2347593 and 2347594. For ESI and crystallographic data in CIF or other electronic format see DOI: https://doi.org/10.1039/d4sc02550d

‡ These authors contributed equally.

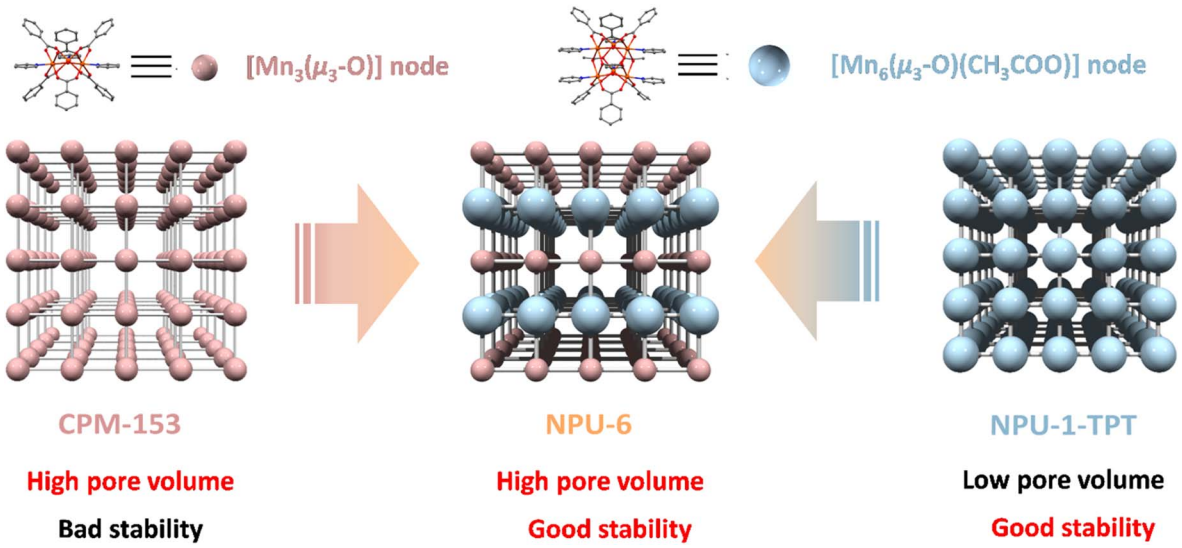

Scheme 1 The ordered assembly of two metal clusters with different chemical nature but the same topological connectivity in one single coordination network to enhance both pore volume and stability.

components, $[Mn_3(\mu_3\text{-}O)]$ and $[Mn_6(\mu_3\text{-}O)_2(CH_3COO)_3]$ clusters, into a single pacs network $[\{Mn_3(\mu_3\text{-}O)\}\{Mn_6(\mu_3\text{-}O)_2(CH_3COO)_3\}(BDC)_6(TPT)_3]$, denoted as **NPU-6**; BDC = benzene-1,4-dicarboxylate; TPT = 2,4,6-tri(4-pyridinyl)-1,3,5-triazine, by controlling the concentration of CH_3COO^-. Single-crystal X-ray diffraction unambiguously determined the ordered arranging of ABAB packing of Mn_3 and Mn_6 cluster layers (Scheme 1).

In addition, by inheriting the high pore volume from **CPM-153** and good thermal stability from **NPU-1-TPT**, **NPU-6** displayed the highest experimental pore volume among these three coordination networks. Consequently, **NPU-6** demonstrated the best C_2H_6/C_2H_4 separation performance among these three coordination networks.

Results

Crystallographic structure of NPU-6

The yellowish hexagonal **NPU-6** single crystal was harvested following a solvothermal reaction of manganese acetate tetrahydrate, TPT, and dicarboxylate ligand H_2BDC in *N*,*N*′-dimethylacetamide (DMA) at 388 K for 3 days. Single-crystal X-ray diffraction data revealed that **NPU-6** crystallizes in a non-centrosymmetric hexagonal space group $P\bar{6}m2$. In this compound, two kinds of metal clusters were observed, the classical trinuclear $[Mn_3(\mu_3\text{-}O)]^{6+}$ cluster and the rare hexanuclear $[Mn_6(\mu_3\text{-}O)_2(CH_3COO)_3]^{6+}$ cluster (Fig. 1a). The charge neutrality of the network indicates the mixed valence state of Mn ions in these clusters, consistent with previous findings and supported by X-ray photoelectron spectroscopy (XPS) analysis (Fig. S2†).[38] Two crystallographically different manganese ions in the asymmetric unit exhibit the same octahedral geometry. Each metal ion coordinated with one μ_3-O atom, one N atom from the TPT ligand, and four O atoms from four carboxylates in a monodentate fashion. Nevertheless, for Mn1 of the $[Mn_3(\mu_3\text{-}O)]$ cluster, all four carboxylates come from four dicarboxylate ligands; meanwhile for Mn2 of the $[Mn_6(\mu_3\text{-}O)_2(CH_3COO)_3]$ cluster, two carboxylates come from two bridging acetate anions, and others from two dicarboxylate ligands. The trinuclear $[Mn_3(\mu_3\text{-}O)]^{6+}$ is constructed from three Mn1 ions bridged by one μ_3-O and six carboxylate groups from the BDC^{2-} ligand, which bares the *syn-syn*-μ^2-η^1:η^1 mode (Fig. S4†), leaving the axial coordination site occupied by the nitrogen atom of the TPT ligand. The distinctive hexanuclear $[Mn_6(\mu_3\text{-}O)_2(CH_3COO)_3]^{6+}$, which was used to build **NPU-1/2/3** in our recent work,[38] is cooperating within **NPU-6**. This hexanuclear node is constructed from six Mn_2 ions, which can be regarded as a face-to-face stack of two trinuclear Mn_3 clusters bridged by three acetate anions with the μ^4-η^2:η^2 mode (Fig. S4†). Each type of cluster is interconnected with three same ones in the *ab* plane by triangular TPT ligands but with six different ones along the *c* axis by BDC^{2-} ligands, further packing as an ABAB mode with an interlayer distance of 0.93 nm (Fig. S5†). Interestingly, the Mn_6 layer contains double-walled TPT ligands because of the connectivity nature of the Mn_6 cluster, while the Mn_3 layer only has single TPT ligand bridging, which would lead to the hyperfine spitting of the pore structures which we will discuss later. Topologically, considering both metal clusters as 9-connected nodes and the TPT ligand as a 3-connected node, the network of **NPU-6** can be described by the point symbol of $\{4^{21}\cdot6^{15}\}\{4^3\}$ with the topology type of pacs (partitioned acs).[41,42] Particularly, such a co-existence of highly connected metal nodes is very rare[43–46] and represents the first example of mixed 9-connected nodes so far. Calculated from the single crystal data based on Platon analysis,[47] **NPU-6** afforded a 3D open network with a porosity of 54.1% and a pore volume of 0.592 $cm^3\ g^{-1}$, lying between the values of **CPM-153** (59.1% and 0.707 $cm^3\ g^{-1}$) and **NPU-1-TPT** (50.6% and 0.514 $cm^3\ g^{-1}$).

The mixed metal cluster assembly results in more complex pore structures, with three types of hierarchical polyhedral cages. For comparison, the same types of cages of **CPM-153**

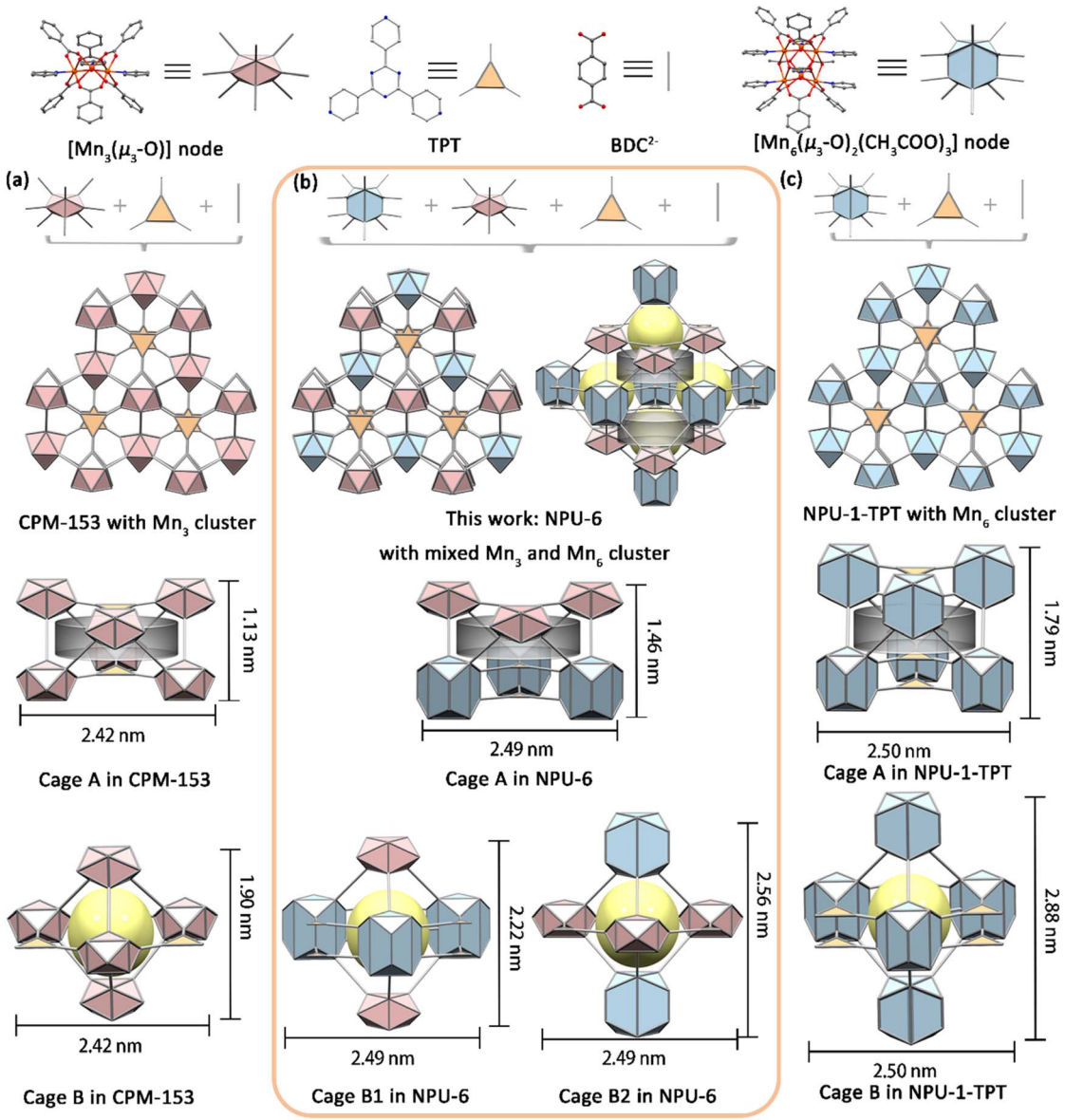

Fig. 1 The comparison of the cages in **CPM-153** (a), **NPU-6** (b) and **NPU-1-TPT** (c). The $[Mn_3(\mu_3\text{-}O)]$ and $[Mn_6(\mu_3\text{-}O)_2(CH_3COO)_3]$ clusters have different chemical structures but the same topological connectivity.

based on the Mn_3 cluster[39,40] and **NPU-1-TPT** based on the Mn_6 cluster are included in Fig. 1a and c. All these structures display two types of cages: cage A with a trigonal antiprism shape and cage B with a trigonal bipyramidal shape. Cage A is surrounded by six metal clusters, six BDC^{2-} ligands and two TPT ligands to form a bicapped trigonal antiprism shaped cage. Because of the larger size of the Mn_6 cluster than the Mn_3 cluster, cage A in **NPU-6** holds medium dimensions (2.49 × 1.46 nm for **NPU-6**; the height was defined by the distances between the C atoms in carboxylate groups and the width was defined by the N atoms coordinated to the metal ions, regardless of the van der Waals radius) between those of **CPM-153** (2.42 × 1.13 nm, Fig. 1a) and **NPU-1-TPT** (2.5 × 1.79 nm, Fig. 1c). Cage B is made of five metal clusters and six BDC^{2-} ligands to afford a trigonal bipyramidal shaped cage. As shown in Fig. 1b, the mixing metal cluster assembly nature in **NPU-6** separates cage B into two different cages (B1 and B2). Cage B1 is constructed by two Mn_3 clusters in the axial direction (2.22 nm) and three Mn_6 clusters in the equatorial plane (2.49 nm). Cage B2 is made of two Mn_6 clusters in the axial direction (2.56 nm) and three Mn_3 clusters in the equatorial plane (2.49 nm). The size of cage B in **CPM-153** is still the lowest one with the dimensions of 2.42 × 1.90 nm. In contrast, cage B in **NPU-1-TPT** has the largest size with the dimensions of 2.50 × 2.88 nm. In **NPU-6**, cage A arranges along the *c* axis and separates each other by bridging tridentate pyridyl ligands. Each cage A interconnects with three B1 cages and three B2 cages by sharing the triangle window formed by BDC^{2-} and TPT ligands. Each cage B1 and cage B2 interconnect with six A cages, affording the overall three-dimensional network (Fig. 1b).

Possible self-assembly mechanism for NPU-6

The unique –A–B–A–B– laminar assembly mode of the tri- and hexa-nuclear clusters in **NPU-6** also led us to consider possible reaction mechanisms. The main difference between trinuclear [$Mn_3(\mu_3\text{-}O)$] clusters and hexanuclear [$Mn_6(\mu_3\text{-}O)_2(CH_3COO)_3$] clusters is that Mn ions are bridged by CH_3COO^- in Mn_6, which was not needed in the Mn_3 cluster. So, the relative concentrations of CH_3COO^- may be the key to the equilibrium shifting from the formation of trinuclear clusters to hexanuclear clusters. With the current scientific and technological means, it is extremely difficult to observe the self-assembly process of molecules at the microscopic scale. On this basis, we propose a reaction mechanism for CH_3COO^- concentration induced assembly (as shown in Fig. 2b). In our proposal, when there is no CH_3COO^- in the reaction system and the product is pure trinuclear based **CMP-153**; when the concentration of CH_3COO^- increases, the hexanuclear cluster begins to form but the formation rate is lower than that of the trinuclear cluster, which leads to the product containing trimer based **CPM-153** and mixed-cluster based **NPU-6**; when the addition of CH_3COO^- is further increased, both clusters form at comparable rates, and here we can harvest mixed-cluster based **NPU-6** as a pure product; when the concentration of CH_3COO^- is further increased, a mixture of hexamer based **NPU-1-TPT** and mixed-cluster based **NPU-6** can be obtained owing to the higher formation rate of hexanuclear midbodies than trinuclear midbodies, and finally we can obtain the hexamer based **NPU-1-TPT** as a pure product with an excess amount of CH_3COO^-. In order to further verify our proposed mechanism and establish the correlation between the content of CH_3COO^- and the result of reaction assembly, a series of experiments were conducted. Firstly, we used manganese acetate tetrahydrate as the metal source and fixed the amount and proportion of metal salts and ligands. When no additional CH_3COOH was added, the extremely low CH_3COO^-

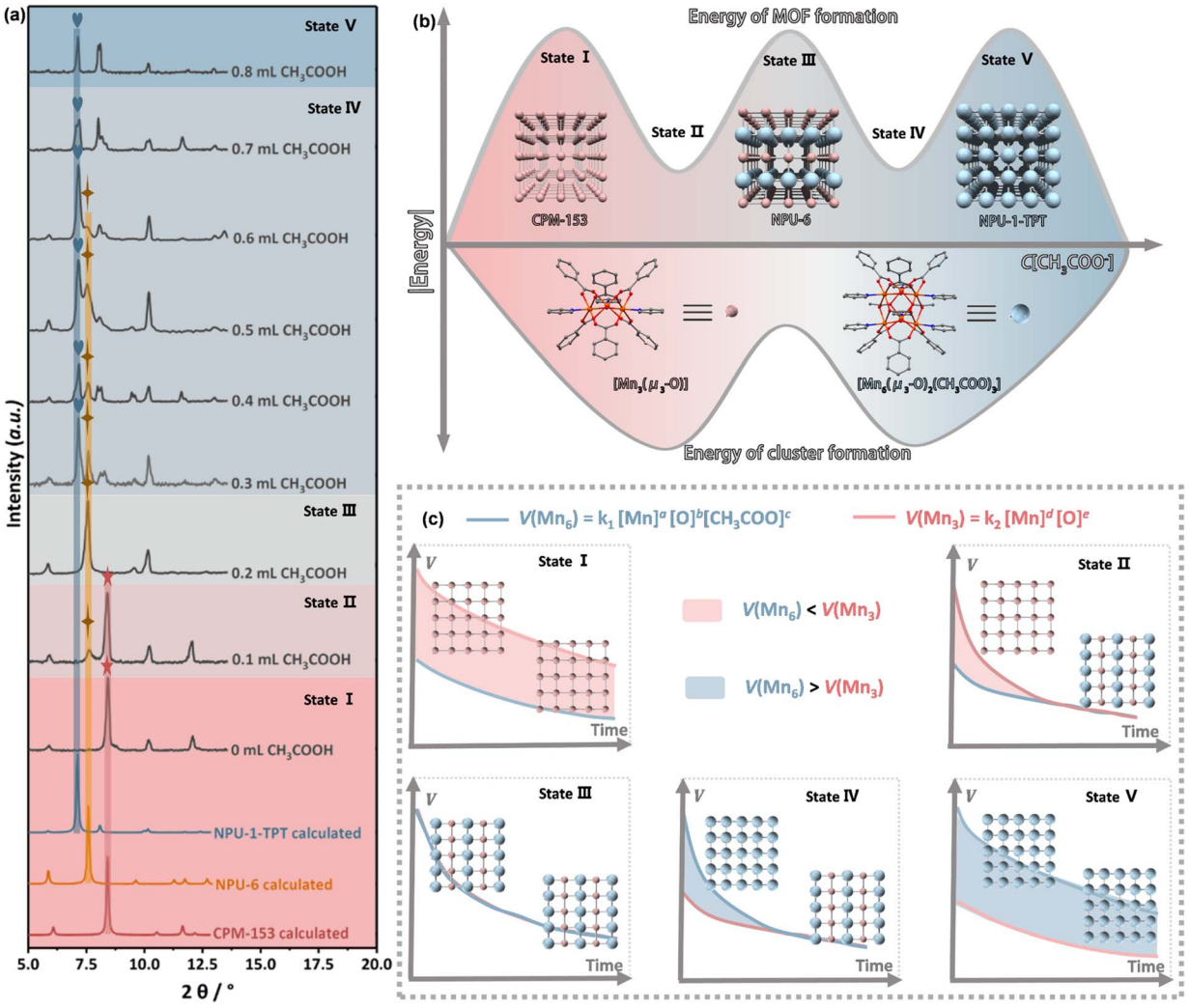

Fig. 2 Precise acetic acid regulation experiment of the reaction system (a) and possible crystal self-assembly mechanism under different conditions ((b) and (c)). (State I) No additional acetic acid is added resulting in pure **CPM-153**; (state II) a small amount of acetic acid results in a mixture of **CPM-153** and **NPU-6**; (state III) microenvironment concentration fluctuation driven assembly mechanism of **NPU-6** when an appropriate amount of acetic acid was added; (state IV) excess acetic acid produces a mixture of **NPU-1-TPT** and **NPU-6**; (state V) pure **NPU-1-TPT** is obtained if acetic acid is far excessive. $\nu(Mn_6)$ is the formation kinetic rate of the [$Mn_6(\mu_3\text{-}O)_2(CH_3COO)_3$] cluster, $\nu(Mn_3)$ is the formation kinetic rate of the [$Mn_3(\mu_3\text{-}O)_2$] cluster.

concentration severely limited the reaction kinetics of the Mn_6 cluster, so only **CPM-153** with the Mn_3 node was generated in the system (Fig. 2a and c state I). When an additional 0.1 mL acetic acid is added, the PXRD of the product showed a strong **CPM-153** peak at 8.37° and a weak **NPU-6** peak at 7.59° (Fig. 2a state II), indicating that a large amount of **CPM-153** and a small amount of **NPU-6** were generated. It is speculated that $\nu(Mn_3)$ in this reaction system is much higher than $\nu(Mn_6)$. During the growth of **CPM-153** with the Mn_3 cluster as the node, a large number of Mn ions are consumed, which further leads to the reduction of $\nu(Mn_3)$. When the kinetic rate of the two metal clusters is the same, alternating self-assembly occurs to generate **NPU-6** (Fig. 2c, state II). As shown in Fig. 2a, when the acetic acid amount increased to 0.2 mL, the concentration of CH_3COOH was sufficient to support the dynamic alternating fluctuation of $\nu(Mn_3)$ and $\nu(Mn_6)$, resulting in the alternating growth of the two metal clusters (as shown in Fig. 2a and c state III), and only the diffraction peak of **NPU-6** appeared in the reaction product. When the additional amount of acetic acid is further increased to 0.3–0.7 mL (Fig. 2a), the situation is opposite to 0.1 mL of CH_3-COOH. At this time, $\nu(Mn_6)$ is much higher than $\nu(Mn_3)$, and **NPU-1-TPT** with hexanuclear Mn_6 as the node is first generated. In this process, a large number of acetic acid ions are consumed, while $\nu(Mn_6)$ gradually decreases to the same as $\nu(Mn_3)$, so that alternate assembly of the two metal clusters occurs in the next stage (Fig. 2c, state IV). When acetic acid is sufficient (0.8 mL), as shown in Fig. 2a, the PXRD pattern of the reaction products only shows the characteristics of **NPU-1-TPT**. This is because sufficient CH_3COO^- makes $\nu(Mn_6)$ much greater than $\nu(Mn_3)$ until the Mn ions are completely consumed, resulting in the formation of only **NPU-1-TPT** with the Mn_6 cluster as the node in the reaction system (Fig. 2c, state V). In summary, as shown in Fig. 2, with the increase of CH_3COOH in the reaction system, the reaction product has 5 different states and follows the change rule of [**CPM-153**]–[**CPM-153** & **NPU-6**]–[**NPU-6**]–[**NPU-6** & **NPU-1-TPT**]–[**NPU-1-TPT**]. In addition, to eliminate the influence of CH_3COO^- of metal salts, we used Mn $(NO_3)_2 \cdot 4H_2O$ as the manganese source to conduct the same experiment, and the PXRD data of the reaction products showed the same trend (Fig. S6†), which further confirmed our proposal. Furthermore, we found that substituting acetic acid with formic acid had the same effect on the reaction, *i.e.*, with the addition of formic acid, the reaction results showed a similar trend (Fig. S7†). Although there is no HBF_4-related component in the single crystal structure, we also designed experiments to explore the effect of HBF_4 on the reaction system. The introduction of HBF_4 can promote the dissolution of the reactants and improve the quality of the crystalline product to a certain extent, but it will not affect the structure of the product (Fig. S7†). These controlled experiments demonstrated that CH_3COOH is the key to the selective nucleation of Mn ions, which provides a reference for the design and synthesis of high nuclear coordination structures in the future.

Functional characterization of NPU-6

It is necessary to evaluate its versatility after realizing the directional and ordered assembly of trinuclear and hexanuclear manganese clusters. In a previous study, we found that **CPM-153** with the traditional Mn_3 cluster has a large theoretical pore capacity but is limited by its poor stability. The expanded **NPU-1-TPT** with Mn_6 clusters has higher stability due to the higher connection number, which prompts us to investigate the stability and adsorption performance of **NPU-6** with hybrid nodes. As shown in Fig. 3a, the powder X-ray diffraction at variable temperature shows that the diffraction peak of **CPM-153** has changed significantly at 90 °C, and the appearance of new diffraction peaks at 9.5° and 14.2° indicates the partial collapse and decomposition of the network. Meanwhile, the powder X-ray diffraction of **NPU-1-TPT** (Fig. 3b) with the hexanuclear cluster has no significant change at 90 °C, and the decrease of the main peak at 280 °C indicates the decomposition of the material. More interestingly, the PXRD patterns show that **NPU-6** (Fig. 3c) with mixed clusters can also be well maintained until 280 °C.

For porous materials, the characterization of porosity can provide more detailed support for their stability research. Therefore, their N_2 adsorption isotherms at 77 K were used to characterize the porosity of the three networks after being treated at different temperatures. To activate the porous material at a lower temperature, the material was soaked with methylene chloride (CH_2Cl_2), and thermogravimetric analysis (TGA) of the as-synthesized and CH_2Cl_2-exchanged samples revealed that the DMA solvent in the pores was completely exchanged by CH_2Cl_2 (Fig. S8†). As shown in Fig. S9–S11,† the three materials showed high porosity after 60 °C treatment under high vacuum, with a reversible type I adsorption isotherm. **CPM-153** with the trinuclear Mn_3 cluster showed a relatively low actual N_2 capacity at 77 K and 100 kPa (255.5 $cm^3\ g^{-1}$) due to the partial collapse of the network after activation. **NPU-1-TPT** with the Mn_6 cluster can be maintained after activation, which results in a moderate N_2 uptake at 77 K and 100 kPa (285.5 $cm^3\ g^{-1}$). Interestingly, **NPU-6** with mixed clusters showed the highest N_2 adsorption capacity under the same conditions (354.1 $cm^3\ g^{-1}$), as the density of the network was effectively reduced by the introduction of Mn_3 clusters. Horvath–Kawazoe (pore geometry: sphere) based pore size distribution analyses were conducted upon the above N_2 sorption isotherms. As shown in Fig. S12,† **CPM-153**, **NPU-1-TPT** and **NPU-6** have a similar pore-size distribution of 0.65–0.90 nm, which is consistent with the aperture obtained from the single crystal data. Assuming that liquid N_2 fills the pores at 77 K and 100 kPa, the pore volume calculated from N_2 absorption at 100 kPa is 0.399 for **CPM-153** with the Mn_3 cluster, 0.447 for **NPU-1-TPT** with the Mn_6 cluster, and 0.552 $cm^3\ g^{-1}$ for the mixed cluster **NPU-6**, which means that **NPU-6** inherits the high theoretical porosity from **CPM-153**. With the increase in processing temperature, the decrease of the measured adsorption capacity of **CPM-153** indicates the rapid collapse of the network, and the porosity of the material almost disappeared when it reached 160 °C (the detailed isotherm is shown in Fig. S13†). Interestingly, the measured N_2 adsorption capacity of **NPU-1-TPT** with the Mn_6 cluster and **NPU-6** with the mixed cluster is almost unchanged even when heated to 180 °C (Fig. 3e, f, S14 and S15†), which means that the introduction of the Mn_6 cluster

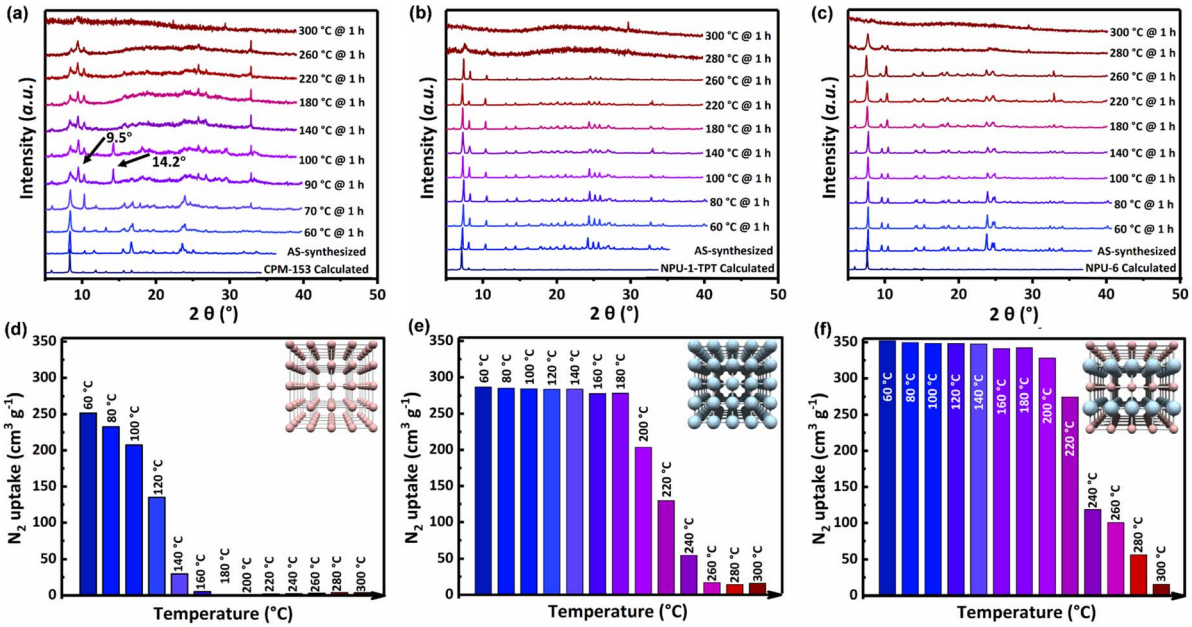

Fig. 3 Stability and porosity tests. PXRD patterns and N_2 uptake data of **CPM-153** ((a) and (d)), **NPU-1-TPT** ((b) and (e)), and **NPU-6** ((c) and (f)) samples after treatment with different temperatures.

makes **NPU-6** inherit the good thermal stability of **NPU-1-TPT**. Further, humidity stability experiments (Fig. S17†) show that **CPM-153** with the Mn_3 cluster collapses rapidly at a relative humidity (R.H.) of 70%, while **NPU-1-TPT** with the Mn_6 cluster and **NPU-6** with the mixed cluster still maintain the complete crystalline state and porosity after 7 days, which indicates that the introduction of the Mn_6 cluster significantly improves the humidity stability of the network. Therefore, after realizing the directional assembly of tri- and hexa-nuclear clusters, **NPU-6** not only has the same stability as **NPU-1-TPT**, but also obtains the highest pore volume, achieving the effect of "1 + 1 > 2".

The high porosity of **NPU-6** prompts us to investigate its C2 adsorption behaviour. As we expected, the adsorption capacity of **CPM-153**, **NPU-1-TPT** and **NPU-6** for C_2H_6 and C_2H_4 increased sequentially (the detailed isotherm is shown in Fig. S18–S20†). As shown in Fig. 4a, at 298 K and 100 kPa, the adsorption capacity of C_2H_6 for **NPU-6** was up to 134.0 $cm^3\ g^{-1}$ (120.1 for C_2H_4), while those of **NPU-1-TPT** and **CPM-153** were 99.8 $cm^3\ g^{-1}$ (91.5 $cm^3\ g^{-1}$ for C_2H_4) and 85.2 $cm^3\ g^{-1}$(79.9 $cm^3\ g^{-1}$ for C_2H_4), respectively. The C_2H_6 uptake of all three materials is greater than that of C_2H_4, implying that they have the potential to purify C_2H_4 from the C_2H_6/C_2H_4 mixture in one step, which prompted us to calculate their IAST (Ideal Adsorbed Solution Theory)[48] selectivity by fitting their adsorption isotherms at 298 K into the Langmuir–Freundlich equation[49] (detailed fitting curves are given in Fig. S21–S23†). As shown in Fig. 4b, **NPU-1-TPT** and **CPM-153** have comparable C_2H_6/C_2H_4 selectivity, while **NPU-6** has the highest selectivity of 1.8. In order to investigate the effect of the simultaneous introduction of two metal clusters on the interaction mechanism of the network with C_2H_6 and C_2H_4, we used molecular simulations to confirm the interaction sites of the materials with C_2H_6 and C_2H_4. As shown in Fig. S24,† the three materials have similar pore characteristics, and C_2H_4 and C_2H_6 are preferentially located on the triangular windows composed of two BDC^{2-} and one TPT ligand. For **NPU-6**, C_2H_6 with a larger size preferentially adsorbs in the middle of the channel compared to the other two materials, and C_2H_6 interacts with eight weak contact sites through four C–H···C (3.41–3.67 Å), two C–H···N (2.90 and 3.07 Å) and two C–H···O (3.39 and 3.39 Å). Meanwhile in **NPU-1-TPT** and **CPM-153**, C_2H_6 tends to bias towards one side of the channel, obtaining seven weak contact points through three C–H···C (3.22–3.74 Å for **CPM-153**; 3.7–3.82 Å for **NPU-1-TPT**), two C–H···N (3.15 and 3.25 Å for **CPM-153**; 3.14 and 3.27 Å for **NPU-1-TPT**) and two C–H···O (3.32 and 3.37 Å for **CPM-153**; 3.69 and 3.71 Å for **NPU-1-TPT**). Due to its smaller molecular size, C_2H_4 tends to act on one side of the channel, forming six weak forces with three C–H···C (3.26–4.05 Å), two C–H···N (2.95 and 3.17 Å), and two C–H···O (3.52 and 3.54 Å) in **NPU-6**, and it is a similar case for **NPU-1-TPT** and **CPM-153**. We reason that C_2H_4 and C_2H_6 are adsorbed in these three materials with minor differences confirmed by the similar binding energy of C_2H_4 ($E_{CPM\text{-}153}$ = 24.69 kJ mol^{-1}, $E_{NPU\text{-}1\text{-}TPT}$ = 25.61 kJ mol^{-1} and $E_{NPU\text{-}6}$ = 24.78 kJ mol^{-1}) and C_2H_6 ($E_{CPM\text{-}153}$ = 30.73 kJ mol^{-1}, $E_{NPU\text{-}1\text{-}TPT}$ = 31.72 mol^{-1} and $E_{NPU\text{-}6}$ = 30.91 kJ mol^{-1}) and the practical separation differences are attributed to the different effective pore volumes of these three materials. To further simulate the realistic separation properties, a single adsorption bed model was built to simulate breakthrough experiments. For these three materials, all the simulating parameters were set the same except for the parameters from isotherms. As shown in Fig. 4d, the first detections of C_2H_4 were found at times of 19.8, 34.0 and 48.7 min for **CPM-153**, **NPU-1-TPT** and **NPU-6**, respectively, in good agreement with the experimental pore volume of **CPM-153** < **NPU-1-TPT** < **NPU-6**. Then, the first observations of 0.5% C_2H_6 in the outlet gas were at 21.3, 35.3 and 53.2 min, respectively. Thus, the retention times

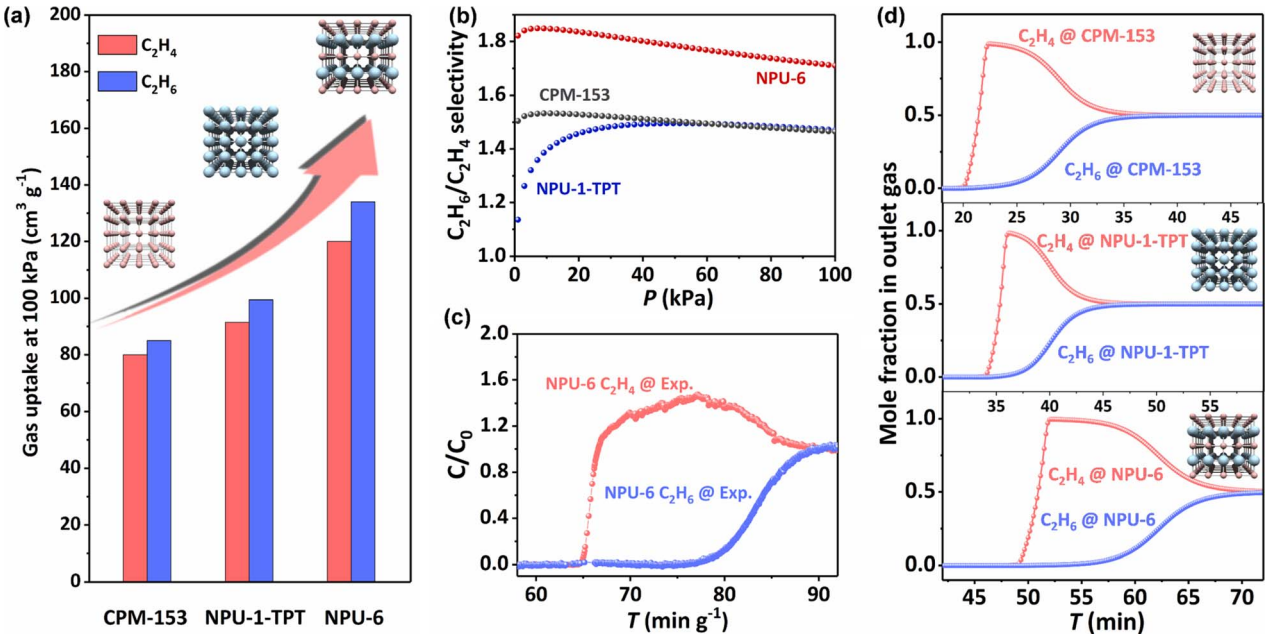

Fig. 4 Characterization of adsorption and separation properties. (a) C_2H_6 and C_2H_4 adsorption capacity of **CPM-153**, **NPU-1-TPT** and **NPU-6** at 298 K and 100 kPa. (b) IAST selectivity of **CPM-153**, **NPU-1-TPT** and **NPU-6**. (c) Experimental breakthrough curves of **NPU-6** at 298 K for C_2H_4/C_2H_6 separation. (d) Simulated breakthrough curves of **CPM-153**, **NPU-1-TPT** and **NPU-6** at 298 K for C_2H_4/C_2H_6 separation.

for the production of polymer-grade C_2H_4 (>99.5%) were 1.5, 1.3 and 4.5 min, in the same order of IAST selectivities of **NPU-1-TPT** < **CPM-153** < **NPU-6**. In a word, by taking advantage of the high pore volume of trimer-based **CPM-153** and the good stability of hexamer-based **NPU-1-TPT**, **NPU-6** displayed the highest capacity as well as the highest selectivity among these three materials in C_2H_4/C_2H_6 separations. Further, as shown in Fig. 4c, the experimental breakthrough curve verified the actual ability of **NPU-6** to produce polymer-grade C_2H_4 from a C_2H_4/C_2H_6 mixture in one step. In order to investigate the separation behaviour of **NPU-6** for a ternary $C_2H_2/C_2H_4/C_2H_6$ mixture (Fig. S25†), we carried out a breakthrough experiment based on a $C_2H_2/C_2H_4/C_2H_6$ ternary gas mixture. As shown in Fig. S20 and S25,† **NPU-6** demonstrates the selective adsorption of C_2H_2 and C_2H_6 over C_2H_4 and further achieves one-step C_2H_4 purification from the ternary gas mixture, but with only limited performance due to the subtle difference in the adsorption capacity of C_2H_4 and C_2H_2 by **NPU-6** at the relatively low-pressure stage. Further, the good cycling stability and regeneration performance were proved by cycling adsorption–desorption experiments (Fig. S26†), in which the C_2H_6 capacity of **NPU-6** did not show any attenuation within five cycles.

Conclusions

In conclusion, we utilized the large chemical difference (size and geometry) of two metal clusters to realize the ordered assembly of such two metal clusters with the same topological connectivity in one single coordination network, through the precise concentration control of the bridging CH_3COO^- ligand in the reaction system. The resulting mixed cluster-assembled coordination network **NPU-6** demonstrates superior stability and high pore volume, and further effective C_2H_6/C_2H_4 separation performance. Subsequent *in situ* characterization experiments for understanding the assembly mechanism of these two metal clusters are under way.

Data availability

The data supporting this article have been included as part of the ESI.† Crystallographic data for **NPU-1-TPT** and **NPU-6** have been deposited at CCDC under 2347593 and 2347594.

Author contributions

K.-J. C. designed the project. J.-W. C. conducted all the experimental work regarding the synthesis, gas adsorption characterisation and breakthrough experiments. T. Z. performed single crystal structure analysis and breakthrough simulation. J.-W. C., T. Z., Y. W., J. C. and K.-J. C. discussed the formation mechanism. T. Z. performed the GCMC calculation. J.-W. C., Y. W. and J.-B. W. performed the collection and analysis of PXRD data. J.-W. C., T. Z., J. C. and K.-J. C. wrote the manuscript, and all authors contributed to the revision of the manuscript.

Conflicts of interest

There are no conflicts to declare.

Acknowledgements

We appreciate the financial support from the National Natural Science Foundation of China (22071195 and 22101231), Youth Innovation Team of Shaanxi Universities, China Postdoctoral Science Foundation (No. 2022M712585), Natural Science Basic

Research Plan in Shaanxi Province of China (2023-YBGY-425 and 2019JQ627), Innovation Foundation for Doctor Dissertation of Northwestern Polytechnical University (CX2022071) and Open Project Program of State Key Laboratory of Inorganic Synthesis and Preparative Chemistry (No. 2024-28). We would like to thank the Analytical & Testing Center of Northwestern Polytechnical University.

Notes and references

1 H. Furukawa, K.-E. Cordova, M. O Keeffe and O.-M. Yaghi, *Science*, 2013, **341**, 1230444.
2 S. Kitagawa, R. Kitaura and S.-i. Noro, *Angew. Chem., Int. Ed.*, 2004, **43**, 2334–2375.
3 J.-J. Perry Iv, J.-A. Perman and M.-J. Zaworotko, *Chem. Soc. Rev.*, 2009, **38**, 1400–1417.
4 D.-J. O'Hearn, A. Bajpai and M.-J. Zaworotko, *Small*, 2021, 2006351.
5 A. Cadiau, K. Adil, P.-M. Bhatt, Y. Belmabkhout and M. Eddaoudi, *Science*, 2016, **353**, 137–140.
6 J.-W. Cao, S. Mukherjee, T. Pham, Y. Wang, T. Wang, T. Zhang, X. Jiang, H.-J. Tang, K.-A. Forrest, B. Space, M.-J. Zaworotko and K.-J. Chen, *Nat. Commun.*, 2021, **12**, 6507.
7 J.-W. Cao, T. Zhang, Y. Wang and K.-J. Chen, *ACS Appl. Mater. Interfaces*, 2024, **16**, 10260–10266.
8 P. Miao, T. Zhang, T. Wang, J. Chen, T. Gao, Y. Wang, J. Kong and K.-J. Chen, *Chin. J. Chem.*, 2022, **40**, 467–474.
9 X. Liu, J. Li, N. Li, B. Li and X.-H. Bu, *Chin. J. Chem.*, 2021, **39**, 440–462.
10 K.-J. Chen, D.-G. Madden, S. Mukherjee, T. Pham, K.-A. Forrest, A. Kumar, B. Space, J. Kong, Q.-Y. Zhang and M.-J. Zaworotko, *Science*, 2019, **366**, 241–246.
11 X. Cui, K.-J. Chen, H. Xing, Q. Yang, R. Krishna, Z. Bao, H. Wu, W. Zhou, X. Dong, Y. Han, B. Li, Q. Ren, M.-J. Zaworotko and B. Chen, *Science*, 2016, **353**, 141–144.
12 S. Zhou, O. Shekhah, A. Ramírez, P. Lyu, E.-A. Hamad, J. Jia, J. Li, P.-M. Bhatt, Z. Huang, H. Jiang, T. Jin, G. Maurin, J. Gascon and M. Eddaoudi, *Nature*, 2022, **606**, 706–712.
13 Y.-Y. Jia, J.-C. Yin, N. Li, Y.-H. Zhang, R. Feng, Z.-Q. Yao and X.-H. Bu, *Chin. J. Chem.*, 2022, **40**, 589–596.
14 H.-L. Zhou, J. Bai, X.-Y. Tian, Z.-W. Mo and X.-M. Chen, *Chin. J. Chem.*, 2021, **39**, 2718–2724.
15 H. Li, M. Eddaoudi, M. O'Keeffe and O.-M. Yaghi, *Nature*, 1999, **402**, 276–279.
16 S.-S.-Y. Chui, S.-M.-F. Lo, J.-P.-H. Charmant, A.-G. Orpen and I.-D. Williams, *Science*, 1999, **283**, 1148–1150.
17 J.-H. Cavka, S. Jakobsen, U. Olsbye, N. Guillou, C. Lamberti, S. Bordiga and K.-P. Lillerud, *J. Am. Chem. Soc.*, 2008, **130**, 13850–13851.
18 G. Ferey, C.-M. Draznieks, C. Serre, F. Millange, J. Dutour, S. Surble and I. Margiolaki, *Science*, 2005, **309**, 2040–2042.
19 H. Furukawa, U. Müller and O.-M. Yaghi, *Angew. Chem., Int. Ed.*, 2015, **54**, 3417–3430.
20 A.-D. Burrows, *CrystEngComm*, 2011, **13**, 3623–3642.
21 X. Kong, H. Deng, F. Yan, J. Kim, J.-A. Swisher, B. Smit, O. M. Yaghi and J. A. Reimer, *Science*, 2013, **341**, 882–885.
22 H. Deng, C. J. Doonan, H. Furukawa, R.-B. Ferreira, J. Towne, C.-B. Knobler, B. Wang and O.-M. Yaghi, *Science*, 2010, **327**, 846–850.
23 M. Inukai, T. Fukushima, Y. Hijikata, N. Ogiwara, S. Horike and S. Kitagawa, *J. Am. Chem. Soc.*, 2015, **137**, 12183–12186.
24 S. Horike, Y. Inubushi, T. Hori, T. Fukushima and S. Kitagawa, *Chem. Sci.*, 2012, **3**, 116–120.
25 T. Fukushima, S. Horike, Y. Inubushi, K. Nakagawa, Y. Kubota, M. Takata and S. Kitagawa, *Angew. Chem., Int. Ed.*, 2010, **49**, 4820–4824.
26 T. Li, Y. Liu, T. Wang, Y. Wu, Y. He, R. Yang and S. Zheng, *Microporous Mesoporous Mater.*, 2018, **272**, 101–108.
27 Z. Dong, Y. Sun, J. Chu, X. Zhang and H. Deng, *J. Am. Chem. Soc.*, 2017, **139**, 14209–14216.
28 A.-M. Fracaroli, P. Siman, D.-A. Nagib, M. Suzuki, H. Furukawa, F.-D. Toste and O.-M. Yaghi, *J. Am. Chem. Soc.*, 2016, **138**, 8352–8355.
29 L.-M. Aguirre-Díaz, F. Gándara, M. Iglesias, N. Snejko, E. Gutiérrez-Puebla and M.-Á. Monge, *J. Am. Chem. Soc.*, 2015, **137**, 6132–6135.
30 L.-J. Wang, H. Deng, H. Furukawa, F. Gándara, K.-E. Cordova, D. Peri and O.-M. Yaghi, *Inorg. Chem.*, 2014, **53**, 5881–5883.
31 Q. Liu, H. Cong and H. Deng, *J. Am. Chem. Soc.*, 2016, **138**, 13822–13825.
32 F. Nouar, T. Devic, H. Chevreau, N. Guillou, E. Gibson, G. Clet, M. Daturi, A. Vimont, J.-M. Grenèche, M. I. Breeze, R. I. Walton, P. L. Llewellyn and C. Serre, *Chem. Commun.*, 2012, **48**, 10237–10239.
33 Z. Ji, T. Li and O.-M. Yaghi, *Science*, 2020, **369**, 674–680.
34 L. Gagliardi and O.-M. Yaghi, *Chem. Mater.*, 2023, **35**, 5711–5712.
35 S.-J. Lee and S.-G. Telfer, *Angew. Chem., Int. Ed.*, 2023, **62**, e2023063.
36 X. Zhao, X. Bu, Q.-G. Zhai, H. Tran and P. Feng, *J. Am. Chem. Soc.*, 2015, **137**, 1396–1399.
37 Y.-S. Wei, M. Zhang, P.-Q. Liao, R.-B. Lin, T.-Y. Li, G. Shao, J.-P. Zhang and X.-M. Chen, *Nat. Commun.*, 2015, **6**, 8348.
38 B. Zhu, J.-W. Cao, S. Mukherjee, T. Pham, T. Zhang, T. Wang, X. Jiang, K.-A. Forrest, M.-J. Zaworotko and K.-J. Chen, *J. Am. Chem. Soc.*, 2021, **143**, 1485–1492.
39 T. Zhang, J.-W. Cao, Y.-F. Dai, H. Feng, S.-Y. Zhang, J. Chen, T. Wang, Y. Wang and K.-J. Chen, *Cryst. Growth Des.*, 2022, **22**, 3594–3600.
40 Q.-G. Zhai, X. Bu, C. Mao, X. Zhao, L. Daemen, Y. Cheng, A. J. Ramirez-Cuesta and P. Feng, *Nat. Commun.*, 2016, **7**, 13645.
41 Q.-G. Zhai, X. Bu, X. Zhao, D.-S. Li and P. Feng, *Acc. Chem. Res.*, 2017, **50**(2), 407–417.
42 V. A. Blatov, *Struct. Chem.*, 2012, **23**, 955–963.
43 F. Nouar, J. F. Eubank, T. Bousquet, L. Wojtas, M. J. Zaworotko and M. Eddaoudi, *J. Am. Chem. Soc.*, 2008, **130**, 1833–1835.
44 A. Schoedel, W. Boyette, L. Wojtas, M. Eddaoudi and M.-J. Zaworotko, *J. Am. Chem. Soc.*, 2013, **135**, 14016–14019.

45 D. Alezi, A. M. P. Peedikakkal, Ł. J. Weseliński, V. Guillerm, Y. Belmabkhout, A. J. Cairns, Z. Chen, Ł. Wojtas and M. Eddaoudi, *J. Am. Chem. Soc.*, 2015, **137**, 5421–5430.
46 B. Tu, Q. Pang, E. Ning, W. Yan, Y. Qi, D. Wu and Q. Li, *J. Am. Chem. Soc.*, 2015, **137**, 13456–13459.
47 A.-L. Spek, *J. Appl. Crystallogr.*, 2003, **36**, 7–13.
48 A.-L. Myers and J.-M. Prausnitz, *AIChE J.*, 1965, **11**, 121–127.
49 A. Dabrowski, J. Oscik, W. Rudzinski and M. Jaroniec, *J. Colloid Interface Sci.*, 1979, **69**, 287–300.